PCCP

Cite this: *Phys. Chem. Chem. Phys.*, 2012, **14**, 10168–10177

www.rsc.org/pccp

PAPER

Understanding of morphology evolution in local aggregates and neighboring regions for organic photovoltaics†

Yu Xie,[a] Ying Bao,[b] Jikai Du,[c] Chaoyang Jiang[b] and Qiquan Qiao*[a]

Received 17th February 2012, Accepted 8th May 2012
DOI: 10.1039/c2cp40503b

Fluorescence intensity and its ratio mapping combined with time-dependent optical microscopy and atomic force microscopy (AFM) were used to understand morphology evolution of local aggregates and neighboring regions for organic solar cells. Three solvents with different boiling points including chlorobenzene (CB), 1,3-dichlorobenzene (1,3-DCB) and 1,2-dichlorobenzene (1,2-DCB) were used to engineer morphology. These solvents affected morphology evolution factors such as solvent evaporation rate, formation (*e.g.*, growth rate, size and/or quantity) of (6,6)-phenyl-C61-butric-acid methyl ester (PCBM)-rich aggregates, and packing/ordering of poly(3-hexylthiophene) (P3HT). Three local regions (1, 2 and 3) including microscale aggregates and their surrounding areas were identified to explore the mechanism of morphology evolution. Region 1 was the PCBM-rich aggregates; region 2 was the PCBM-deficient area; and region 3 was the area composed of a relatively normal P3HT/PCBM composite beyond region 2 for each solvent. The intensity of fluorescence spectra decreased as region 1 > region 2 > region 3 in thermally annealed (140 °C, 20 min) P3HT/PCBM blend film from each solvent. The highest fluorescence intensity in region 1 was probably caused by the relatively poor phase separation where both PCBM and P3HT formed large isolated domains. The higher fluorescence intensity ratio (720 nm/650 nm) suggested a larger relative amount of PCBM molecules, supported by similar morphologies in fluorescence intensity ratio mapping compared to those in optical images. The fluorescence intensity ratio was with the order of region 1 > region 3 > region 2 in both CB and 1,3-DCB based films, but with region 1 > region 2 > region 3 for the 1,2-DCB based film. The order of effective area taken up by aggregates was CB > 1,3-DCB > 1,2-DCB in annealed (140 °C, 10 min) bulk blend films. The final solar cell performance agreed with morphology results. This work is imperative with regards to revealing the mechanism of morphology evolution in local aggregates and surrounding regions for organic photovoltaic films.

1. Introduction

Organic photovoltaics (OPVs) have attracted extensive attention due to their technological potential for inexpensive fabrication processing, mechanical flexibility, and light weight in organic semiconductors.[1–8] Conjugated polymer based bulk heterojunction (BHJ) cells are made from intimate blends of electron donors and acceptors with interpenetrating networks (highly percolated phase).[1,2,9] BHJ solar cells using low bandgap polymers have achieved efficiencies beyond 8%.[10] Although polymer based tandem solar cell efficiency has achieved 10.6%, a module efficiency of 10% or above for organic photovoltaics is still preferred for commercial applications.[11] To achieve this goal, efforts are needed to focus on optimization of active layer morphology, design of new donor and acceptor materials, and/or use of multi-junction structure to further increase cell efficiencies.[12–18] Among these, engineering of active layer morphology is an important factor affecting BHJ solar cell performance. Active layer morphology is affected by many factors such as spin casting solvents, blend compositions, concentrations of solutions, annealing conditions (thermal and solvent annealing), and polymer chemical structures (*e.g.* region-regular and region-random).[12,19–24]

A pioneering study of active layer morphology was based on poly[2-methoxy-5-(2′-ethyl-hexyloxy)-1,4-phenylene vinylene]/buckminsterfullerene (MEH-PPV/C_{60}) blend films, in which isolated C_{60} phase was observed.[12,25] Later, the morphology

[a] *Center for Advanced Photovoltaics, Department of Electrical Engineering & Computer Science, South Dakota State University, Brookings, SD 57006, USA. E-mail: Qiquan.Qiao@sdstate.edu*
[b] *Department of Chemistry, University of South Dakota, Vermillion, SD 57069*
[c] *Department of Mechanical Engineering, South Dakota State University, Brookings, SD 57006, USA*

† Electronic supplementary information (ESI). Additional optical images, dark field image, red emission image, fluorescence mappings, fluorescence intensity ratio (720 nm/650 nm) mappings, fluorescence spectra at different locations, AFM amplitude images and photo of samples. See DOI: 10.1039/c2cp40503b.

study was extended to poly[(2-methoxy-5-(3′,7′-dimethyl-octyloxy))-*p*-phenylene vinylene] (MDMO-PPV)/(6,6)-phenyl-C61-butric-acid methyl ester (PCBM) blend films.[26] Poly(3-hexylthiophene) (P3HT)/PCBM is one of the most common blends for OPV devices, and its morphology has been extensively studied.[27,28] Annealing treatment showed significant impact on both film morphology and device efficiency.[29] Some of our contributed works reported solvent effects only on P3HT/PCBM blend films' nanomorphology with/without photovoltaic performances.[30,31] In addition to the study on two-dimensional (2D) surface morphology, three-dimensional (3D) morphology has been explored directly *via* electron tomography and confocal optical microscopy, revealing deeper information on morphology.[32–35] Several reports have suggested that nanomorphology extending from a few nanometers (nm) to tens of nanometers could offer a more fundamental understanding of the relationship between active layer morphology and solar cell performance. In these reports, advanced scattering methods were used to provide statistical information on general structural ordering and crystallinity.[36,37] The above discussions have been focused on nanoscale morphology of blend films.

Several other groups have reported microscale morphology studies. Microscale morphology of P3HT/PCBM films and growth of crystalline domains depend on P3HT regio-regularity[38] and annealing conditions such as time and temperature.[39,40] Recently, trace solvent effects on the morphology of P3HT/PCBM blend films have been reported.[41] PCBM domains ranging from dot-like to rod-like structures were observed in both dichlorobenzene (DCB) and chlorobenzene (CB) based samples.

Although a number of papers have been published about solvent effects on morphologies including PCBM aggregation and P3HT packing/ordering, to the best of our knowledge, the formation mechanism of local aggregates and their neighboring regions has not been fully understood yet. The observations revealed by confocal optical microscopy and fluorescence mapping may provide new insight into P3HT/PCBM blend films, particularly into the composition and structures of the local aggregates as well as the neighboring regions. In addition, scanning probe microscopy measurement has offered nanoscale gradient analysis on regions identified by microscale observations. Unlike some previous reports, this work connects microscale aggregations with nanoscale morphologies in P3HT/PCBM blend films, as well as their influences on solar cell performances. Organic solar cells with different morphologies induced by the three solvents were also fabricated and characterized.

2. Experimental section

2.1. Film preparation and characterization

Regio-regular P3HT (rrP3HT) with an average molecular weight of ~50 K was purchased from Rieke Metals Inc.[31] Mixtures of P3HT and PCBM (Nano-C Inc) were dissolved in different solvents at ~1.0 wt% (~1 : 1 wt/wt) to make blend solutions. Three solvents, CB, 1,3-DCB and 1,2-DCB, were used to prepare their respective solutions. Their chemical structures are shown in Scheme 1. Blend films were made by spin-coating P3HT/PCBM solutions (with 0.25 μm filters) at

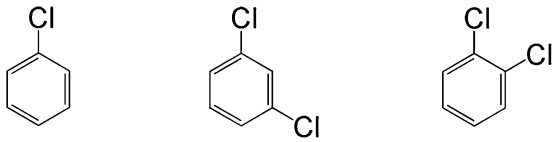

Chlorobenzene 1, 3-Dichlorobenzene 1, 2-Dichlorobenzene

Scheme 1 Chemical structures of chlorobenzene (CB), 1,3-chlorobenzene (1,3-DCB), and 1,2-chlorobenzene (1,2-DCB).

100/800 rpm for ~40 s (two steps) on quartz plates or other substrates for optical microscopy, fluorescence mapping, absorption spectra and nanoscale morphology measurements. These films were left wet and then dried in covered glass Petri-dishes for solvent annealing. Thermal annealing was performed at 140 °C for 0, 5, 10 and 20 min. Pure P3HT films were also deposited from ~1.0 wt% P3HT solutions in such solvents as comparison with similar procedures for P3HT/PCBM blend films. Absorbance spectra of blend films were recorded by an Agilent 8453 UV-vis spectrophotometer.

2.2. Optical microscopy observations

Optical images with a large area were taken by Keyence VK-9700 color 3D laser scanning microscope with color charge-coupled devices (CCD) image sensor under ambient temperature. The light source was a 100 W halogen lamp. Image connection function was a seamless high-precision large-area mode. The arrangement for the observation was a pinhole confocal optical system. Optical images for local regions were obtained on an Olympus BX41 microscope using a 50× objective lens (NA = 0.75) and recorded with a three megapixel CCD camera.

2.3. Fluorescence intensity and ratio mapping, and fluorescence spectra

All fluorescence related data were acquired on a scanning confocal microscope (Aramis, Horiba Jobin Yvon Inc, Edison, NJ) equipped with a diode-pumped solid-state (DSPP) laser (532 nm). The laser was focused onto samples with an intensity of 0.17 μW using a 50× objective lens (NA 0.75) and the samples were mounted onto a 200 × 200 × 200 μm piezo scanner. Fluorescence spectra were collected with the same objective under a 180° back-scattering configuration and passed through an edge filter into a monochromater and electric-cooled CCD camera. To obtain a fluorescence map, an array of fluorescence spectra was collected when the laser was raster scanned across a selected area of a sample. Fluorescence spectra were acquired for 0.3 s at each pixel. The spectra were then mathematically processed, and the intensity distribution of fluorescence peaks of interest can be revealed. The fluorescence ratio mapping was obtained through a software LabSpec.

2.4. Atomic force microscopy (AFM) characterization

AFM images of P3HT/PCBM films were taken by an Agilent 5500 AFM/SPM microscope. A Si tip (Budget Sensors, Multi 75*E*-G, resonant frequency: 75 Hz, force constant: 3 N m^{-1}) coated with Pt/Cr conductive coating was used for measurements *via* tapping mode. The scanning probe microscopy (SPM) software Gwyddion was used to analyze AFM images.

2.5. Photovoltaic devices fabrication and characterization

ITO glasses (Delta Technology, Inc) were cleaned by ultrasonic treatment in detergent, deionized water, acetone and isopropyl alcohol (~99.5%) sequentially 10 min for each, followed by O_2 plasma treatment.[31] Afterward, a thin layer of poly(3,4-ethylenedioxythiophene) : poly(styrenesulfonate) (PEDOT : PSS, AI 4083) was spin-coated onto the cleaned ITO substrates at 4000 rpm for ~30 s in air. The samples were then baked at 140 °C for 20 min to remove residue water and then transferred into a glove box. Similar procedures were used to make active layers for morphology study and device fabrication. Top electrodes Ca/Al were constructed in high vacuum (less than 5×10^{-6} mbar) *via* a thermal evaporator. Post thermal annealing was performed at 140 °C for 10 min.

Current density–voltage (*J–V*) plots were taken by an Agilent 4155C and a Keithley 2400 source generator under illuminations of a solar simulator (Xenon lamp, Newport) with an intensity of ~100 mW cm^{-2} (AM 1.5).[31] A Hamamatsu mono-crystalline Si cell certificated by the National Renewable Energy Laboratory (NREL) was applied to calibrate *J–V* measurements.[42] Incident photon-to-electron conversion efficiency (IPCE) measurements were carried out *via* a set of M-QE kit system (Newport) with an Oriel cornerstone monochromator.[31,42,43]

3. Results and discussion

3.1. Optical microscopy observations

Optical microscopy was used to study the microscale morphology of P3HT/PCBM blend films. Fig. 1 shows images (200 × 200 μm) of P3HT/PCBM blend films from CB, 1,3-DCB, and 1,2-DCB, respectively. These solvents were used due to their different boiling points: 131 (CB), 173 (1,3-DCB), and 180.5 °C (1,2-DCB). This affected the thermal annealing induced morphology formation processes such as solvent evaporation rate, growth (*e.g.*, size and quantity) of PCBM-rich aggregates, PCBM-deficient region, and packing/ordering of P3HT, based on our observations (Table 1).

As shown in Fig. 1a–c, no obvious microscale aggregates were observed in P3HT/PCBM blend films prior to thermal treatments. Also, in the initial 5 min thermal annealing period, no significant microscale aggregates (Fig. 1d–f) were formed, which is consistent with a previous report by Jo *et al.*[40] After annealing for 10 and 20 min, needle-like aggregates formed with increasing size and/or quantity in all films with time (Fig. 1g–l). These microscale aggregates have previously been confirmed as PCBM-rich domains by various tools such as Raman scattering,[44] X-ray diffraction,[45] AFM,[46] transmission electron microscopy and selected-area electron diffraction.[45,47,48] During thermal annealing, the residual solvent was evaporated and PCBM molecules moved to aggregation sites, forming PCBM-rich domains.[40] To further confirm this, optical images (200 × 200 μm) of annealed (140 °C, 10 min) pure P3HT films from CB, 1,3-DCB, and 1,2-DCB were recorded and shown in Fig. S1a–c (see ESI†). In contrast to the images (Fig. 1g–i) from annealed (140 °C, 10 min) P3HT/PCBM blend films, no needle-like aggregates were observed in annealed pure P3HT films regardless of the selection of solvents. This suggested that microscale aggregates grew due to an introduction of PCBM, further supporting that they were PCBM-rich domains.

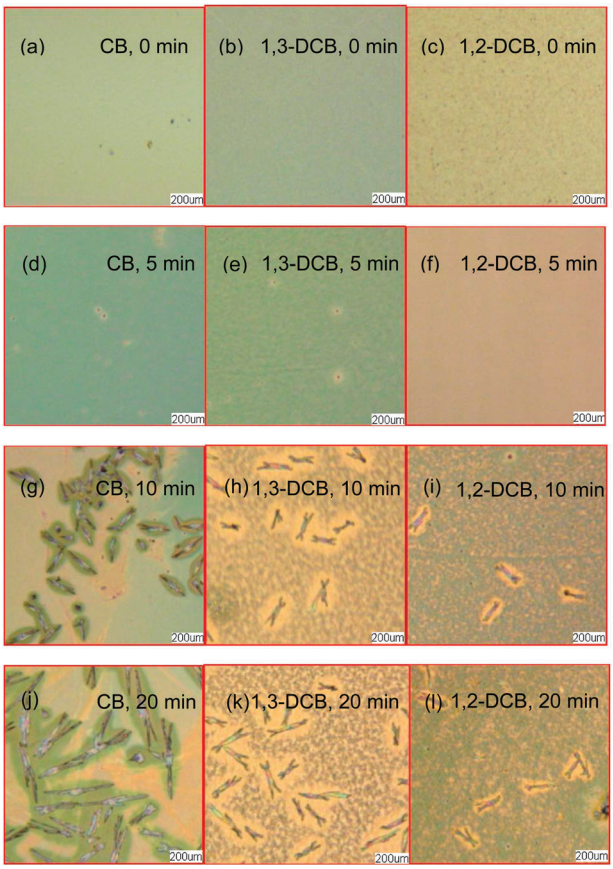

Fig. 1 Time-dependent optical images of P3HT/PCBM blend films with different solvents and thermal annealing time at 140 °C. (a) CB, 0 min; (b) 1,3-DCB, 0 min; (c) 1,2-DCB, 0 min; (d) CB, 5 min; (e) 1,3-DCB, 5 min; (f) 1,2-DCB, 5 min; (g) CB, 10 min; (h) 1,3-DCB, 10 min; (i) 1,2-DCB, 10 min; (j) CB, 20 min; (k) 1,3-DCB, 20 min; (l) 1,2-DCB, 20 min. Image size: 200 × 200 μm.

By comparing aggregates processed from different solvents annealed for 10 and 20 min, the CB based film exhibited the largest size and/or quantity of aggregates, while the 1,2-DCB based film showed the smallest size and/or quantity of aggregates. This suggested that the order of solvent effect upon PCBM aggregation rate was CB > 1,3-DCB > 1,2-DCB. Different boiling points of solvents can cause different aggregation rates, therefore leading to deviations in aggregate size and/or quantity.[29,40] Among the three solvents, CB has the lowest

Table 1 Solvent induced variations in the factors affecting morphology evolution

Boiling point	CB < 1,3-DCB < 1,2-DCB
Solvent evaporation rate	CB > 1,3-DCB > 1,2-DCB
Microscale aggregate growth rate	CB > 1,3-DCB > 1,2-DCB
Microscale aggregate size and/or quantity	CB > 1,3-DCB > 1,2-DCB
Packing/ordering of P3HT in region 3	CB < 1,3-DCB < 1,2-DCB

boiling point and hence, the fastest drying process due to its higher solvent evaporation rate. Such a high evaporation rate provided an earlier saturated PCBM environment in the CB based film, compared with other two solvents. This environment allowed aggregates to start growing at an earlier time. Therefore, aggregates had a longer time to grow in the CB based film than those in the other two films even with the same annealing time. This was consistent with the fluorescence ratio imaging that PCBM was more deficient around aggregates in the CB based film than in the other two films, which will be discussed below. Similarly, compared with 1,3-DCB, a lower evaporation rate in 1,2-DCB contributed partly to a smaller size and/or quantity of aggregates.

The difference in boiling point between 1,3-DCB and 1,2-DCB is quite small (less than 8 °C), and can not be used to convincingly explain the large differences in morphology and device performance (Section 3.5). Another reason affecting microscale aggregate formation was the PCBM solubility due to the solvent polarity.[31,32] The deviation of solubility from the three solvents can be induced from their considerable difference in solvent polarity (dipole moment, CB: ~1.61; 1,3-DCB: ~1.55; 1,2-DCB: ~2.30 D).[49] 1,2-DCB should show a higher solubility for PCBM than CB and 1,3-DCB, and this higher solubility has been reported previously in the case of CB.[31,50] The same case might be true for 1,3-DCB. Therefore, PCBM can be homogeneously dissolved in solutions and distributed in films from 1,2-DCB. Relatively large PCBM clusters resulting from lower solubility might retard P3HT packing/ordering however, they can be prevented in 1,2-DCB. The difference in polarity and solubility between 1,3-DCB and 1,2-DCB could cause large differences in morphology and device performance.

The polymer packing/ordering in the 1,2-DCB based film was enhanced. Such pronounced P3HT packing was another factor causing the smaller size and/or quantity of aggregates in 1,2-DCB. Jo *et al.* previously reported that the highly ordered packing of P3HT chains suppressed the diffusion of PCBM molecules and limited the growth of microscale PCBM-rich aggregates.[40] They reported that smaller anisotropy (*e.g.*, aspect ratio) of aggregates indicated an improved polymer packing order.[40] As shown in Fig. 1j–l, the anisotropy order of aggregates in different films was CB > 1,3-DCB > 1,2-DCB. This implied that P3HT packing/ordering was the weakest in the CB based film, but strongest in the 1,2-DCB based film of these cases.

In real photovoltaic devices, top electrodes play an important role for the morphological evolution on active layers. Previous work reported that top electrodes could trap trace solvent within active layers and as a result PCBM molecules might diffuse at a higher rate and bigger aggregates generated.[41] However, the other work reported that double-sided or sandwich-like confinement (between top electrodes and PEDOT:PSS coated substrates) could reduce the diffusion of PCBM molecules and crystallization rate of microscale aggregates during thermal annealing, leading to circular aggregates.[51] In our work we focused on the morphology study from different solvents. Due to the limitations of our facility we could not remove Ca/Al layers first for studying directly the case of morphology under top electrodes. This was acceptable since our focus here was the microscale study on PCBM aggregate growth in P3HT/PCBM blend films from different solvents (CB, 1,2-DCB, and 1,3-DCB).

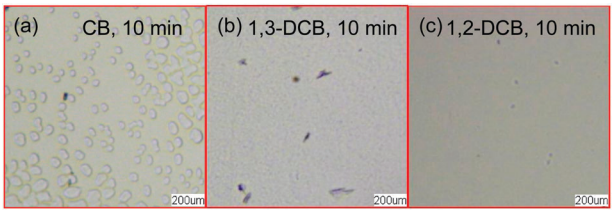

Fig. 2 Optical images (200 × 200 μm) of aggregates in active layers (annealed at 140 °C, 10 min, with top electrodes) from (a) CB, (b) 1,3-DCB and (c) 1,2-DCB.

The microscale morphology of active layers with top electrodes after post-annealing at 140 °C for 10 min is shown in Fig. 2. With the top electrode of Ca/Al deposited, the size and anisotropy of aggregates with Ca/Al electrodes (Fig. 2a–c) decreased compared with those without electrodes (Fig. 1g–i). This indicated that the Ca/Al electrode can confine the aggregation growth by reducing the crystallization rate of microscale aggregates during thermal annealing, which is consistent with previous reports.[51] Although the large aggregates shown in Fig. 1g–i might not represent the morphology of P3HT/PCBM films in real photovoltaic devices because the top electrode of Ca/Al was not deposited, the order of effective area size taken up by aggregates was found to be CB > 1,3-DCB > 1,2-DCB (Fig. 2), which was the same as the one explored with the exposed P3HT/PCBM layer for each solvent.

3.2. Absorption spectra

The P3HT packing order was confirmed by absorption spectra in blend films. Fig. 3 shows normalized absorption spectra of annealed (140 °C, 10 min) P3HT/PCBM films processed from CB, 1,3-DCB and 1,2-DCB, respectively. The vibronic peak at ~610 nm originated from interchain-delocalized excitation (resulting from strong π-stacking of polymer chains) and correlated with the degree of P3HT packing/ordering.[41,52,53] The peak height at ~610 nm in normalized absorption spectra was with the order of CB < 1,3-DCB < 1,2-DCB. This suggested that 1,3-DCB and 1,2-DCB induced a higher P3HT packing than CB.[54,55] The 1,3-DCB based films occasionally showed higher vibronic peaks (~610 nm) than the 1,2-DCB based films, but most measurements exhibited the opposite result. This indicated a high possibility of the strongest P3HT packing in the 1,2-DCB

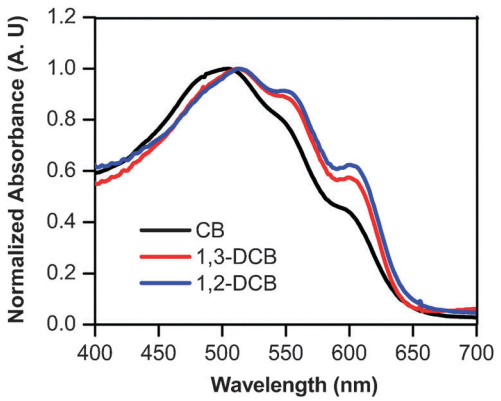

Fig. 3 Normalized absorption spectra of P3HT/PCBM blend films from CB, 1,3-DCB, and 1,2-DCB after thermal annealing (140 °C, 10 min).

based films in these cases. The higher boiling point, slower film drying/growth process, and higher solubility of PCBM contributed to the enhanced P3HT packing.[31,44,56]

3.3. Fluorescence intensity and ratio mapping, and fluorescence spectra

Fig. 4 shows local optical images (50 × 50 μm), fluorescence images, and fluorescence spectra of annealed (140 °C, 20 min) P3HT/PCBM films from CB, 1,3-DCB, and 1,2-DCB, respectively. As shown in optical images (Fig. 4a–c), regions 1, 2, and 3 were identified. Region 1 was the PCBM-rich aggregate locations; region 2 was the area around aggregate locations; region 3 was far enough from region 1 to be considered as relatively normal P3HT/PCBM composite for each solvent (Note: a "relatively normal P3HT/PCBM composite" does not imply a well-organized P3HT packing and a homogeneously percolated phase separation).

Fluorescence studies at these local regions under the same excitation intensity and wavelength (532 nm) provided deep understanding of the aggregate growth mechanism. PCBM molecules approached region 1 from nearby and/or underneath, a proposition supported by a previous report.[57] This left behind more "pure" P3HT regions in the PCBM-deficient zones. Ballantyne *et al.* reported that PCBM aggregates showed much higher fluorescence intensity than the neighboring regions.[58] Fluorescence intensities from the three regions (1, 2 and 3) of our samples were also different and increased from region 3 < region 2 < region 1. Fluorescence intensity images (Fig. 4d–f)

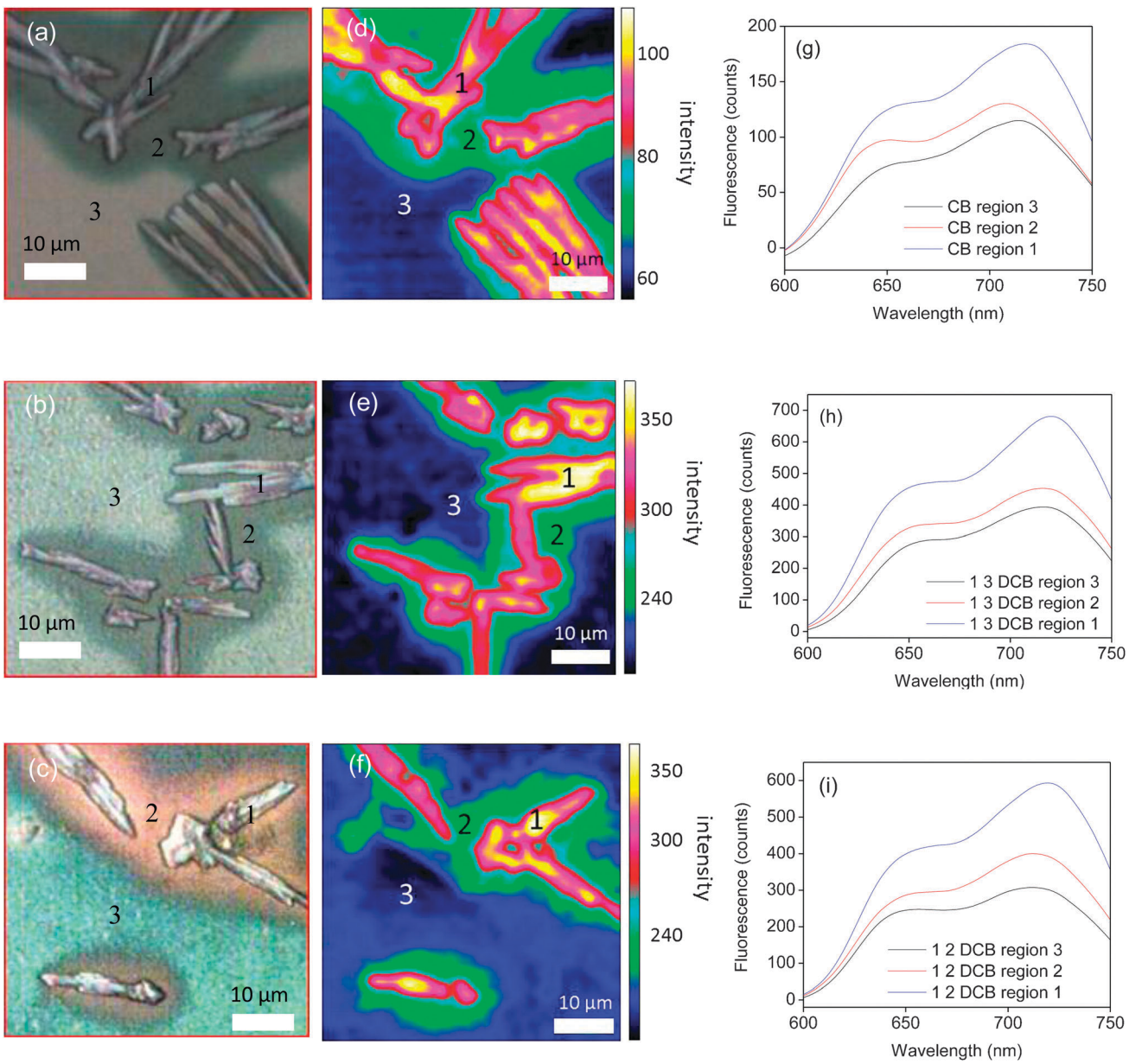

Fig. 4 Thermally annealed (140 °C, 20 min) P3HT/PCBM blend films: local optical microscopy images from (a) CB, (b) 1,3-DCB, and (c) 1,2-DCB; fluorescence images (excitation: 532 nm) from (d) CB, (e) 1,3-DCB, and (f) 1,2-DCB; and fluorescence spectra (excitation: 532 nm) from (g) CB, (h) 1,3-DCB, and (i) 1,2-DCB. Optical and fluorescence image size: 50 × 50 μm; scale bar: 10 μm.

showed that region 1 exhibited much higher intensity than region 3 in thermally annealed (140 °C, 20 min) P3HT/PCBM blend films from each solvent, consistent with the previous report.[58]

Fig. 4g–i show fluorescence spectra of films processed from CB, 1,3-DCB, and 1,2-DCB, respectively. Both P3HT and PCBM molecules show absorption at 532 nm.[55,59] Two fluorescence peaks were found with one centered at ~650 nm and the other at ~700–720 nm. As reported by others,[58] the peak at ~650 nm was from P3HT, while that at ~700–720 nm was contributed from both P3HT and PCBM molecules.[42,58] The highest fluorescence intensity at ~650 nm appeared in the PCBM-rich aggregates (region 1) because both PCBM and P3HT formed their respective large isolated domains. PCBM formed PCBM-rich aggregates in region 1, while P3HT self-assembled into P3HT-rich packed structures surrounding the aggregates.[38,57] This led to an inefficient phase separation for charge transfer between P3HT and PCBM and thus a weak fluorescence quenching in region 1. Region 2 showed a lower fluorescence intensity at ~650 nm than region 1. Compared with region 1, region 2 was PCBM-deficient, but the remaining isolated PCBM molecules (not big domains) could still cause quenching. Region 3 was far from the aggregates and therefore, P3HT and PCBM were relatively normally dispersed in region 3 for each film. For both CB and 1,3-DCB based films, the fluorescence ratio mapping (Fig. 5) suggested that the relative amount (ratio) of PCBM in region 3 was larger than region 2, causing a stronger fluorescence quenching between P3HT and PCBM (lower fluorescence intensity at ~650 nm) in region 3. The fluorescence ratio mapping (Fig. 5) also suggested that the 1,2-DCB based film exhibited a lower ratio of PCBM in region 3 than region 2. However, Fig. 4i shows a lower fluorescence intensity at ~650 nm in region 3, which might be caused by an improved P3HT packing order (Fig. 7c) in region 2. Such improved P3HT packing can push PCBM molecules out of P3HT chains,[57] and reduce fluorescence quenching.

The fluorescence peak at ~700–720 nm was contributed by both P3HT and PCBM molecules.[42,58] Like that at ~650 nm, similar reason could cause the fluorescence intensity order of region 1 > region 2 > region 3 at ~700–720 nm for the part contributed from P3HT. For the contribution which originated from PCBM, region 1 showed the largest PCBM aggregates since PCBM moved to it from neighboring regions (Fig. 4d–f). Region 2 might have a smaller size of PCBM aggregates compared to region 1 as P3HT self-assembled into packed structures and pushed some of the remaining PCBM molecules away to form such aggregated structures.[57] Region 3 was beyond the PCBM-deficient regions and therefore P3HT and PCBM were still relatively normally dispersed, which was supported by AFM images discussed in the next section. In addition, the order of quenching (region 3 > region 2 > region 1), which might be caused by hole transfer from PCBM to P3HT, could be explained by the same reason (enhanced P3HT packing can push PCBM away and reduce quenching) for the quenching of P3HT-generated fluorescence. Therefore, the same fluorescence intensity order at ~700–720 nm might be induced. If considering other factors such as self-quenching, the case could be complicated, which was not discussed for simplicity.

In order to study solvent effects on PCBM movement and aggregation mechanism for different blend films during thermal annealing, fluorescence intensity ratio mapping of emission at 720 nm *vs.* that at 650 nm were recorded and shown in Fig. 5. As mentioned above, the emission peak at 650 nm is only from P3HT, while that at 720 nm is partly from PCBM.[58] This ratio (720 nm/650 nm) mapping was used to roughly estimate the relative amounts of PCBM and P3HT, if other effects on fluorescence such as packing in P3HT and PCBM were ignored. The morphologies in fluorescence intensity ratio mapping (Fig. 5) were very similar to those in optical microscopy images and fluorescence mapping (Fig. 4), supporting the assumption that a higher fluorescence intensity ratio suggested a larger relative amount of PCBM molecules in these cases.

The fluorescence intensity ratio (720 nm/650 nm) was with the order of region 1 > region 3 > region 2 in both CB and 1,3-DCB based films (Fig. 4a and b), but with region 1 > region 2 > region 3 for the 1,2-DCB based film (Fig. 5c). In both CB and

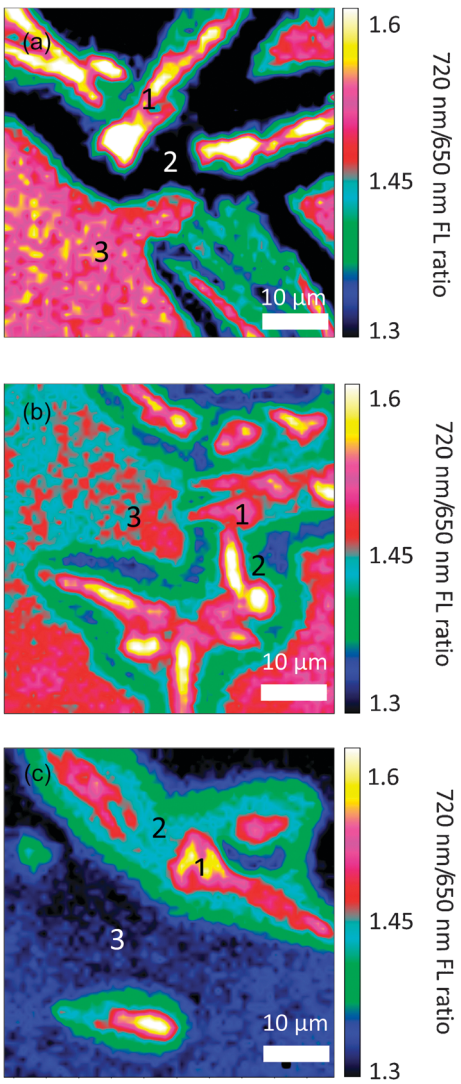

Fig. 5 Fluorescence intensity ratio (720 nm/650 nm) mapping of thermally annealed (140 °C, 20 min) P3HT/PCBM blend films from (a) CB, (b) 1,3-DCB, and (c) 1,2-DCB. Image size: 50 × 50 μm, scale bar: 10 μm, excitation: 532 nm.

1,3-DCB based films, region 1 exhibited the highest fluorescence intensity ratio (720 nm/650 nm), reflecting the largest relative amount of PCBM molecules at such locations. However, region 2 showed the lowest fluorescence intensity ratio, suggesting that it was PCBM-deficient with the least relative amount of PCBM molecules among the three zones. Since region 3 was beyond the PCBM-rich and PCBM-deficient zones, there was only a little PCBM added or removed and thereby the relative amount of PCBM in region 3 was between regions 1 and 2 for such two cases.

In contrast to both the CB and 1,3-DCB based films, region 2 exhibited a higher fluorescence intensity ratio (720 nm/650 nm) than region 3 in the 1,2-DCB based film. This suggested a higher relative amount of PCBM in region 2 than region 3 in the film. 1,2-DCB has the highest boiling point (180.5 °C) and thereby leads to the slowest solvent evaporation rate. This kept the 1,2-DCB based film "wet" for the longest time among P3HT/PCBM blend films from each solvent. The "wet" film led to a slower formation of a saturation environment, which delayed the precipitation of aggregation centers. In addition, enhanced P3HT packing and higher PCBM solubility also reduced the aggregate growth rate. These caused the slowest aggregation rate in blend films from each solvent. Therefore the usage of PCBM at region 2 for region 1 was much less in the 1,2-DCB based film. This could account for the least PCBM decrease in region 2 of the 1,2-DCB based film among P3HT/PCBM blend films from each solvent.

Such a "wet" environment with residual solvent in the 1,2-DCB based film offered a longer time for P3HT to self-assemble into a more ordered structure, retarding the diffusion of PCBM. This was supported by optical images (Fig. 1) for the growth of aggregates. However, trace solvent in active layers may also help PCBM molecules to diffuse at a higher rate, based on a prior report.[41] There might be a balance for PCBM diffusion.

3.4. AFM images

Due to the limitations of microscale measurement, AFM images were used to study solvent induced variations on nanoscale morphology. Fig. 6 shows AFM phase images (1 × 1 μm) at region 3 of annealed (140 °C, 10 min) P3HT/PCBM blend films processed from CB, 1,3-DCB, and 1,2-DCB, respectively. Compared with both CB and 1,3-DCB based films, the 1,2-DCB based film exhibited a more intimate P3HT/PCBM mixture with a more self-assembled organized structure. This agreed well with the improved P3HT chain packing/ordering indicated by the higher vibronic peaks (~610 nm) from 1,2-DCB in the UV-vis absorption spectra (Fig. 3). In one of our earlier reports,[31] surface AFM phase images and bright field transmission electron microscopy (TEM) images showed that 1,2-DCB based P3HT/PCBM films exhibited a more homogeneous distribution and a better-ordered phase separation than CB based films.[31] Such prior results provided some solvent effect information on nanomorphology in P3HT/PCBM blend films and supported the surface observations (AFM) and UV-vis absorption spectra performed in this work. Compared with CB and 1,3-DCB, the slow evaporation rate of 1,2-DCB provided a more "wet" environment with residual solvent and a longer time for P3HT to self-assemble into a more ordered structure. Additionally, a higher solubility of

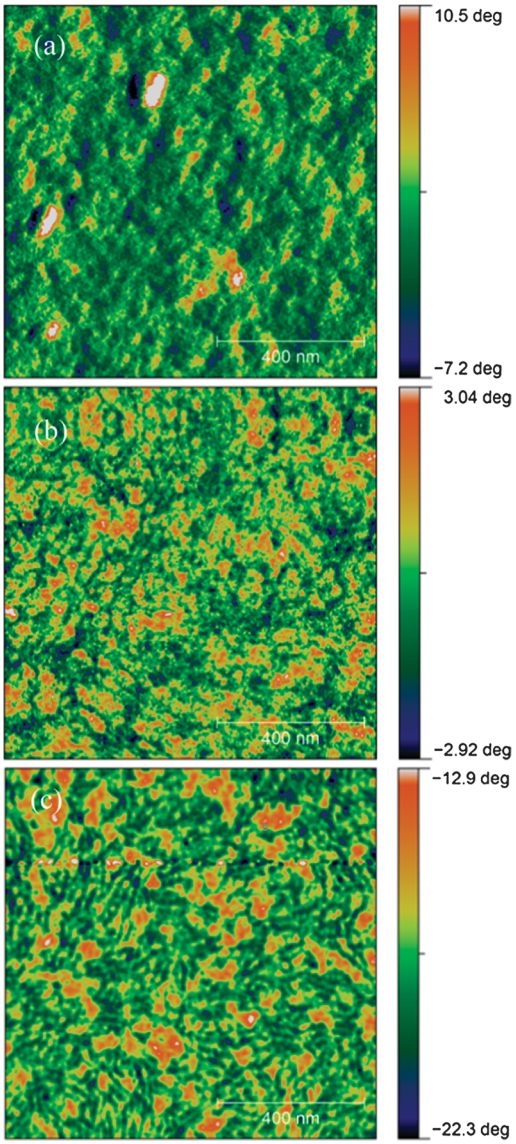

Fig. 6 AFM phase images in region 3 of annealed (140 °C, 10 min) P3HT/PCBM blend films from (a) CB, (b) 1,3-DCB, and (c) 1,2-DCB. Image size: 1 × 1 μm, scale bar: 400 nm.

PCBM in 1,2-DCB can also induce the formation of small nanodomains and a relatively well-organized phase percolation.[31,50]

The improved phase separation was discussed in the AFM section, while the improved carrier transport pathway in 1,2-DCB based films was evidenced by the local hole mobility measurement reported previously.[31] Hole mobilities of 4.64×10^{-3} and 1.4×10^{-2} cm^2 V^{-1} s^{-1} were reported on blend films processed from CB and 1,2-DCB, respectively.[31] The relatively high hole mobility in the 1,2-DCB based film was partly attributed to the strongest P3HT packing/ordering, indicating the most continuous possible pathway for hole transport. This could be proved by series resistance (R_s) discussed below. Such nanoscale morphology with homogeneously ordered packing connected well with the microscale morphology where the aggregate grew with small anisotropy.

To more accurately correlate AFM with fluorescence ratio (720 nm/650 nm) mapping, phase images in region 2 were

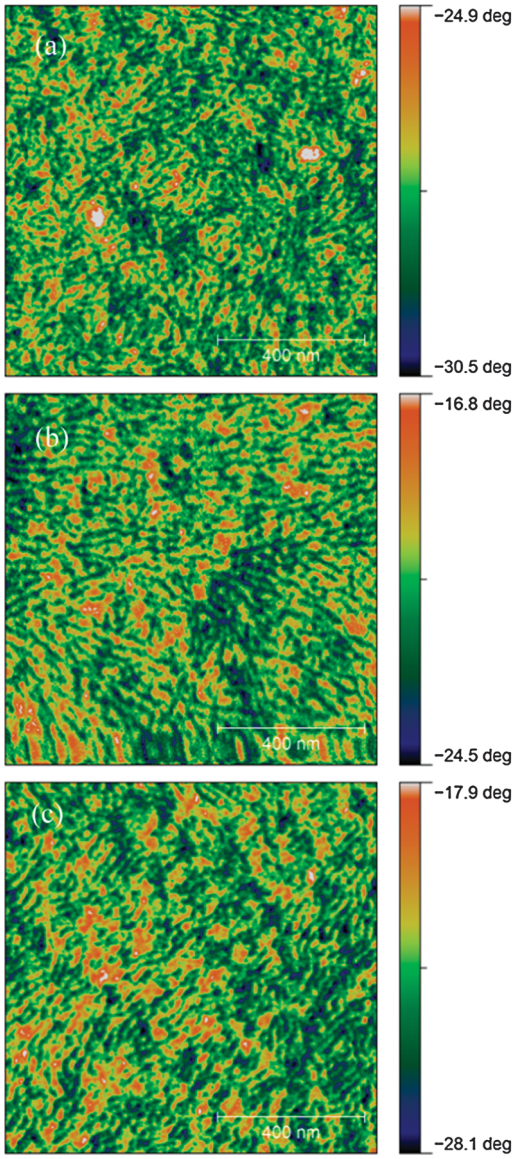

Fig. 7 AFM phase images in region 2 of annealed (140 °C, 10 min) P3HT/PCBM blend films from (a) CB, (b) 1,3-DCB, and (c) 1,2-DCB. Image size: 1 × 1 μm, scale bar: 400 nm.

investigated and shown in Fig. 7. Compared with images in region 3 of the blend films, images in region 2 showed more self-assembled organized structures. This suggested an improved P3HT chain packing/ordering in these films.

3.5. Photovoltaic devices

Fig. 8 shows current density-voltage (J–V) curves and incident photon-to-electron conversion efficiency (IPCE) spectra of the annealed (140 °C, 10 min) devices processed from CB, 1,3-DCB, and 1,2-DCB, respectively. To the best of our knowledge, 1,3-DCB has been seldom reported for BHJ photovoltaic devices.[29,30] Solar cell performance was summarized in Table 2. As shown in Fig. 8a, the 1,2-DCB based cell yielded the highest efficiency (η) of 3.5% with an open circuit voltage (V_{oc}) of 0.52 V, short circuit current density (J_{sc}) of 11.4 mA cm^{-2} and fill factor (FF) of 59%, while the CB based device exhibited

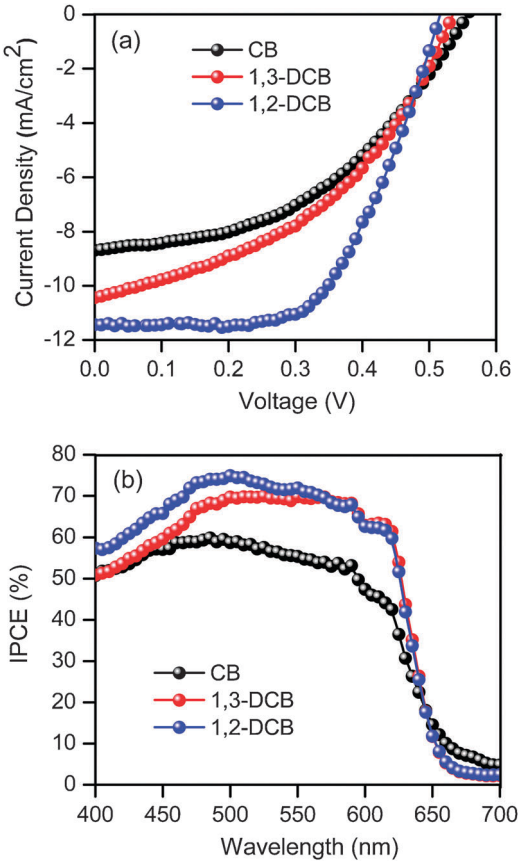

Fig. 8 (a) Current density-voltage (J–V) curves and (b) incident photon-to-electron conversion efficiency (IPCE) of devices processed from CB, 1,3-DCB, and 1,2-DCB, respectively.

Table 2 Performance summary of devices processed from CB, 1,3-DCB and 1,2-DCB (n = 1.2 for J–V fitting)

	V_{oc} (V)	J_{sc} (mA cm^{-2})	FF (%)	η (%)	R_s (Ω cm^2)
CB	0.56	8.7	45	2.2	23.5
1,3-DCB	0.54	10.4	43	2.4	14.1
1,2-DCB	0.52	11.4	59	3.5	8.9

the lowest η of 2.2% with a V_{oc} of 0.56 V, J_{sc} of 8.7 mA cm^{-2}, and FF of 45%. The IPCE maximum was ~60, 70 and 75% for cells from CB, 1,3-DCB, and 1,2-DCB, respectively (Fig. 8b), in agreement with the order of J_{sc}.

The highest η was caused by the high values of J_{sc} and FF, which was partly attributed to the enhanced phase separation in the 1,2-DCB based film. Region 3 showed larger surface area than regions 2 and 1 in blend films. The enhanced phase separation with the order of CB < 1,3-DCB < 1,2-DCB in region 3 has been discussed in Fig. 6. This was further supported by series resistance (R_s) calculated from their J–V curves. R_s was 23.5, 14.1, and 8.9 Ω cm^2 for each cell from CB, 1,3-DCB, and 1,2-DCB, respectively. Li *et al.* reported that slow growth of dry films with improved P3HT ordering/crystallinity could increase hole mobility and keep a balanced charge transport between electrons and holes, resulting in a high FF.[56] Prior work also reported that BHJ blend films from the solvent with a lower boiling point displayed an increased

tendency for poor phase separation (less intermixing between donor and acceptor) but higher domain purity, which could increase charge recombination with a lower solar cell efficiency.[36]

As shown by Fig. 2, the significantly enlarged and more numerous microscale aggregates in the CB based film might retard P3HT ordering/crystallinity, decrease interfacial donor/acceptor area, cause electrical defect sites on carrier transport and increase series resistance. Large PCBM-rich aggregates could damage PCBM/metal interfaces.[48] Previous work reported that high photocurrents were found in locations free of microscale aggregates while low photocurrents found in microscale aggregate districts.[41] In addition, as the size and/or quantity of microscale aggregates got smaller in blend films with top electrodes from CB to 1,3-DCB to 1,2-DCB, the effective device surface area enhanced.[38] The solar cell performance agreed with results from morphology observations and absorption spectra.

Both FF values and V_{oc} of these devices were not as high as the best results in the literature. To obtain good working devices, electrons are required to transport to electrodes over distances of 100–500 nm.[60] One report showed a ~400 nm electron diffusion length in PCBM-rich composites of a MDMO-PPV : $PCBM_{0.75}/TiO_2$ blend.[61] Exciton diffusion length in PCBM was suggested to be ~5 nm.[62]

Fig. S6 (see ESI†) shows aggregates' absolute vertical height (Z values) in active layers with top electrodes after post-annealing at 140 °C for 10 min. The height of aggregates was estimated by gaps of relatively vertical dimensions. Aggregates' Z values in CB based and 1,3-DCB based films with top electrodes were up to several μm in scale (Fig. S6a–c, ESI†) while the one in 1,2-DCB based films of the scale of a few hundred nm (Fig. S6d, ESI†). Based on these Z values, it was difficult for electrons to penetrate aggregates and reach electrodes. This implied somewhat high R_s for solar cells (Table 2), leading to relatively low FF values. V_{oc} decreased as CB > 1,3-DCB > 1,2-DCB in these cases. This might be caused by the improved P3HT ordering/crystallinity, which could shift P3HT's highest occupied molecular orbitals (HOMO) upward and then reduce V_{oc}. This is consistent with a previously reported paper.[40] However, these voltages were still in a normal range for P3HT/PCBM solar cells. Additionally, these devices were fabricated under the same conditions. The comparison among them showed a trend of solvent effects, which was reasonable. This work can provide a new insight in understanding cell performance factors such as interfaces and morphologies.

4. Conclusions

In conclusion, both the mechanism and solvent effects on morphology evolution in local aggregates and neighboring regions in organic photovoltaic films during thermal annealing were understood with a deep insight by time-dependent optical microscopy, fluorescence intensity and its ratio mapping (720 nm/650 nm), and AFM gradient analysis. Three regions (1, 2 and 3) including microscale aggregates and surrounding areas were identified. Region 1 was the PCBM-rich aggregate area; region 2 was the PCBM-deficient zone; and region 3 was the area composed of relatively normal P3HT/PCBM composite. The intensity of the fluorescence spectra decreased in the order of region 1 > region 2 > region 3 in thermally annealed (140 °C, 20 min) P3HT/PCBM blend films from each solvent. The highest fluorescence intensity in region 1 was caused by the relatively poor phase separation where both PCBM and P3HT formed large isolated domains. The fluorescence intensity ratio (720 nm/650 nm) was of the order of region 1 > region 3 > region 2 in both CB and 1,3-DCB based films, but of region 1 > region 2 > region 3 for the 1,2-DCB based film. Region 1 exhibited the highest fluorescence ratio and suggested the largest relative amount of PCBM. The effective area taken up by aggregates exhibited an order of CB > 1,3-DCB > 1,2-DCB in annealed (140 °C, 10 min) blend films both with and without top electrodes. The enhanced phase separation and P3HT packing in region 3 were observed with the order of CB < 1,3-DCB < 1,2-DCB. The final three solar cells' performance was consistent with the above results. Unlike some other works,[30,31] this report connected microscale morphology with nanoscale morphology in P3HT/PCBM blend films, as well as their possible influences on solar cell performance.

Acknowledgements

This material is based upon work partially supported by the NSF/EPSCoR (Grant No. 0903804) and SD BoR CRGP, NSF CAREER (ECCS-0950731), NASA EPSCoR (NNX09AP67A), US-Israel Binational Science Foundation (2008265), and US-Egypt Joint Science & Technology Funds (913). We acknowledge Mr L. Loen from Department of Mechanical Engineering at South Dakota State University for his help for optical microscopy. Y. B. is grateful for the support from NSF (DGE-0903685) and Sigma Xi Grant-in-Aid of Research program.

References

1 A. Tamayo, T. Kent, M. Tantitiwat, M. A. Dante, J. Rogers and T. Q. Nguyen, *Energy Environ. Sci.*, 2009, **2**, 1180–1186.
2 S. Swaraj, C. Wang, H. P. Yan, B. Watts, L. N. Jan, C. R. McNeill and H. Ade, *Nano Lett.*, 2010, **10**, 2863–2869.
3 S. B. Darling, *Energy Environ. Sci.*, 2009, **2**, 1266–1273.
4 H. Zhang and J. Ouyang, *Appl. Phys. Lett.*, 2010, **97**, 063509.
5 D. S. Yu, Y. Yang, M. Durstock, J. B. Baek and L. M. Dai, *ACS Nano*, 2010, **4**, 5633–5640.
6 J. Li, M. Yan, Y. Xie and Q. Qiao, *Energy Environ. Sci.*, 2011, **4**, 4276–4283.
7 A. Loiudice, A. Rizzo, L. De Marco, M. R. Belviso, G. Caputo, P. D. Cozzoli and G. Gigli, *Phys. Chem. Chem. Phys.*, 2012, **14**, 3987–3995.
8 B. C. Popere, A. M. Della Pelle, A. Poe and S. Thayumanavan, *Phys. Chem. Chem. Phys.*, 2012, **14**, 4043–4057.
9 J. Zhao, S. Bertho, J. Vandenbergh, G. Van Assche, J. Manca, D. Vanderzande, X. Yin, J. Shi, T. Cleij, L. Lutsen and B. Van Mele, *Phys. Chem. Chem. Phys.*, 2011, **13**, 12285–12292.
10 R. F. Service, *Science*, 2011, **332**, 293–293.
11 N. Choudhury, PV-Tech, http://www.pv-tech.org/news/ucla_researchers_reach_10.6_efficiency_for_tandem_polymer_solar_cells, accessed 16th February, 2012.
12 H. Hoppe and N. S. Sariciftci, *J. Mater. Chem.*, 2006, **16**, 45–61.
13 J. Gilot, M. M. Wienk and R. A. J. Janssen, *Adv. Mater.*, 2010, **22**, E67–E71.
14 M. Siddiki, J. Li, D. Galipeau and Q. Qiao, *Energy Environ. Sci.*, 2010, **3**, 867–883.
15 T. Xu and Q. Qiao, *Energy Environ. Sci.*, 2011, **4**, 2700–2720.
16 S. C. Price, A. C. Stuart, L. Q. Yang, H. X. Zhou and W. You, *J. Am. Chem. Soc.*, 2011, **133**, 4625–4631.
17 I. Botiz, R. D. Schaller, R. Verduzco and S. B. Darling, *J. Phys. Chem. C*, 2011, **115**, 9260–9266.

18 M. Siddiki, S. Venkatesan and Q. Qiao, *Phys. Chem. Chem. Phys.*, 2012, **14**, 4682–4686.
19 C. V. Hoven, X. D. Dang, R. C. Coffin, J. Peet, T. Q. Nguyen and G. C. Bazan, *Adv. Mater.*, 2010, **22**, E63–E66.
20 S. H. Park, A. Roy, S. Beaupre, S. Cho, N. Coates, J. S. Moon, D. Moses, M. Leclerc, K. Lee and A. J. Heeger, *Nat. Photonics*, 2009, **3**, 297–302.
21 G. Li, V. Shrotriya, Y. Yao, J. S. Huang and Y. Yang, *J. Mater. Chem.*, 2007, **17**, 3126–3140.
22 R. Giridharagopal and D. S. Ginger, *J. Phys. Chem. Lett.*, 2010, **1**, 1160–1169.
23 S. E. Shaheen, C. J. Brabec, N. S. Sariciftci, F. Padinger, T. Fromherz and J. C. Hummelen, *Appl. Phys. Lett.*, 2001, **78**, 841–843.
24 M. T. Rispens, A. Meetsma, R. Rittberger, C. J. Brabec, N. S. Sariciftci and J. C. Hummelen, *Chem. Commun.*, 2003, 2116–2118.
25 C. Y. Yang and A. J. Heeger, *Synth. Met.*, 1996, **83**, 85–88.
26 H. Hoppe, T. Glatzel, M. Niggemann, A. Hinsch, M. C. Lux-Steiner and N. S. Sariciftci, *Nano Lett.*, 2005, **5**, 269–274.
27 H. W. Tang, G. H. Lu, L. G. Li, J. Li, Y. Z. Wang and X. N. Yang, *J. Mater. Chem.*, 2010, **20**, 683–688.
28 D. H. Wang, S. H. Im, H. K. Lee, O. O. Park and J. H. Park, *J. Phys. Chem. C*, 2009, **113**, 17268–17273.
29 S. Markutsya, C. Y. Jiang, Y. Pikus and V. V. Tsukruk, *Adv. Funct. Mater.*, 2005, **15**, 771–780.
30 Y. Xie, P. Dutta, D. Cengher, V. Bommisetty, J. Li, D. Galipeau and Q. Qiao, *Organic Photovoltaics X, Proc. SPIE.*, 2009, 7416, 74161Q.
31 P. Dutta, Y. Xie, M. Kumar, M. Rathi, P. Ahrenkiel, D. Galipeau, Q. Qiao and V. Bommisetty, *J. Photonics Energy*, 2011, **1**, 011124.
32 S. van Bavel, E. Sourty, G. de With, S. Veenstra and J. Loos, *J. Mater. Chem.*, 2009, **19**, 5388–5393.
33 S. S. van Bavel, E. Sourty, G. de With and J. Loos, *Nano Lett.*, 2009, **9**, 507–513.
34 B. V. Andersson, A. Herland, S. Masich and O. Inganas, *Nano Lett.*, 2009, **9**, 853–855.
35 J. H. Huang, F. C. Chien, P. L. Chen, K. C. Ho and C. W. Chu, *Anal. Chem.*, 2010, **82**, 1669–1673.
36 W. Chen, T. Xu, F. He, W. Wang, C. Wang, J. Strzalka, Y. Liu, J. Wen, D. J. Miller, J. Chen, K. Hong, L. Yu and S. B. Darling, *Nano Lett.*, 2011, **11**, 3707–3713.
37 B. A. Collins, J. R. Tumbleston and H. Ade, *J. Phys. Chem. Lett.*, 2011, **2**, 3135–3145.
38 C. H. Woo, B. C. Thompson, B. J. Kim, M. F. Toney and J. M. J. Frechet, *J. Am. Chem. Soc.*, 2008, **130**, 16324–16329.
39 M. Campoy-Quiles, T. Ferenczi, T. Agostinelli, P. G. Etchegoin, Y. Kim, T. D. Anthopoulos, P. N. Stavrinou, D. D. C. Bradley and J. Nelson, *Nat. Mater.*, 2008, **7**, 158–164.
40 J. Jo, S. S. Kim, S. I. Na, B. K. Yu and D. Y. Kim, *Adv. Funct. Mater.*, 2009, **19**, 866–874.
41 L. Chang, H. W. A. Lademann, J.-B. Bonekamp, K. Meerholz and A. J. Moulé, *Adv. Funct. Mater.*, 2011, **21**, 1779–1787.
42 Y. Xie, Y. Li, L. Xiao, Q. Qiao, R. Dhakal, Z. Zhang, Q. Gong, D. Galipeau and X. Yan, *J. Phys. Chem. C*, 2010, **114**, 14590–14600.
43 Y. Xie, P. Joshi, S. B. Darling, Q. Chen, T. Zhang, D. Galipeau and Q. Qiao, *J. Phys. Chem. C*, 2010, **114**, 17880–17888.
44 J. Catalan and J. Elguero, *J. Am. Chem. Soc.*, 1993, **115**, 9249–9252.
45 P. Vanlaeke, A. Swinnen, I. Haeldermans, G. Vanhoyland, T. Aernouts, D. Cheyns, C. Deibel, J. D'Haen, P. Heremans, J. Poortmans and J. V. Manca, *Sol. Energy Mater. Sol. Cells*, 2006, **90**, 2150–2158.
46 D. Chirvase, J. Parisi, J. C. Hummelen and V. Dyakonov, *Nanotechnology*, 2004, **15**, 1317–1323.
47 A. Swinnen, I. Haeldermans, M. vande Ven, J. D'Haen, G. Vanhoyland, S. Aresu, M. D'Olieslaeger and J. Manca, *Adv. Funct. Mater.*, 2006, **16**, 760–765.
48 T. J. Savenije, J. E. Kroeze, X. Yang and J. Loos, *Adv. Funct. Mater.*, 2005, **15**, 1260–1266.
49 C. P. Smyth and S. O. Morgan, *J. Am. Chem. Soc.*, 1927, **49**, 1030–1038.
50 L.-M. Chen, Z. Hong, G. Li and Y. Yang, *Adv. Mater.*, 2009, **21**, 1434–1449.
51 X. Yang, A. Alexeev, M. A. J. Michels and J. Loos, *Macromolecules*, 2005, **38**, 4289–4295.
52 R. Österbacka, C. P. An, X. M. Jiang and Z. V. Vardeny, *Science*, 2000, **287**, 839–842.
53 U. Zhokhavets, T. Erb, G. Gobsch, M. Al-Ibrahim and O. Ambacher, *Chem. Phys. Lett.*, 2006, **418**, 347–350.
54 X. M. Jiang, R. Osterbacka, O. Korovyanko, C. P. An, B. Horovitz, R. A. J. Janssen and Z. V. Vardeny, *Adv. Funct. Mater.*, 2002, **12**, 587–597.
55 V. Shrotriya, J. Ouyang, R. J. Tseng, G. Li and Y. Yang, *Chem. Phys. Lett.*, 2005, **411**, 138–143.
56 G. Li, V. Shrotriya, J. S. Huang, Y. Yao, T. Moriarty, K. Emery and Y. Yang, *Nat. Mater.*, 2005, **4**, 864–868.
57 R. A. Marsh, J. M. Hodgkiss, S. Albert-Seifried and R. H. Friend, *Nano Lett.*, 2010, **10**, 923–930.
58 A. M. Ballantyne, T. A. M. Ferenczi, M. Campoy-Quiles, T. M. Clarke, A. Maurano, K. H. Wong, W. Zhang, N. Stingelin-Stutzmann, J.-S. Kim, D. D. C. Bradley, J. R. Durrant, I. McCulloch, M. Heeney, J. Nelson, S. Tierney, W. Duffy, C. Mueller and P. Smith, *Macromolecules*, 2010, **43**, 1169–1174.
59 J. A. Mikroyannidis, A. N. Kabanakis, S. S. Sharma and G. D. Sharma, *Adv.Funct. Mater.*, 2011, **21**, 746–755.
60 N. D. Treat, M. A. Brady, G. Smith, M. F. Toney, E. J. Kramer, C. J. Hawker and M. L. Chabinyc, *Adv. Energy Mater.*, 2011, **1**, 82–89.
61 P. A. C. Quist, T. J. Savenije, J. M. Schins, J. E. Kroeze, P. A. Rijkers and L. D. A. Siebbeles, *Phys. Rev. B: Condens. Matter Mater. Phys.*, 2007, **75**, 195317.
62 G. F. Burkhard, E. T. Hoke, S. R. Scully and M. D. McGehee, *Nano Lett.*, 2009, **9**, 4037–4041.